AIP | Applied Physics Letters

Optical sectioning by wide-field photobleaching imprinting microscopy

Chiye Li, Liang Gao, Yan Liu, and Lihong V. Wang

Citation: Applied Physics Letters **103**, 183703 (2013); doi: 10.1063/1.4827535
View online: http://dx.doi.org/10.1063/1.4827535
View Table of Contents: http://scitation.aip.org/content/aip/journal/apl/103/18?ver=pdfcov
Published by the AIP Publishing

Optical sectioning by wide-field photobleaching imprinting microscopy

Chiye Li,[a] Liang Gao,[a] Yan Liu, and Lihong V. Wang[b]
Optical Imaging Laboratory, Department of Biomedical Engineering, Washington University in St. Louis, One Brookings Dr., St. Louis, Missouri 63130, USA

(Received 10 September 2013; accepted 8 October 2013; published online 29 October 2013)

We present a generic wide-field optical sectioning scheme, photobleaching imprinting microscopy (PIM), for depth-resolved cross-sectional fluorescence imaging. Wide-field PIM works by extracting a nonlinear component that depends on the excitation fluence as a result of photobleaching-induced fluorescence decay. Since no specific fluorescent dyes or illumination modules are required, wide-field PIM is easy to implement on a standard microscope. Moreover, wide-field PIM is superior to deconvolution microscopy in removing background fluorescence, yielding a six-fold improvement in image contrast. © *2013 AIP Publishing LLC*.
[http://dx.doi.org/10.1063/1.4827535]

Three-dimensional fluorescence microscopy is an indispensable tool in studying cell and tissue biology.[1] However, because of out-of-focus light, conventional wide-field fluorescence microscopy generally does not have sectioning capabilities. To achieve depth-resolved wide-field fluorescence imaging, two major strategies are commonly used. One strategy, referred to as deconvolution microscopy (DM), computationally determines how much out-of-focus light is expected for the optics in use and then seeks to redistribute this light to its points of origin in the sample.[2] However, the reduction of out-of-focus light by DM is effective only for specimens in which the ratio of background fluorescence to the in-focus signal is no greater than ~20:1.[3] Additionally, the contrast improvement by DM is achieved at the expense of a decreased signal-to-noise ratio and may also introduce structural artifacts.[4] The second strategy, referred to as structured illumination microscopy (SIM), projects a grid excitation pattern onto the sample and captures three phase-shifted fluorescence images.[5,6] The sectioned image is then calculated by a demodulation algorithm.[7] The drawback of SIM lies in image artifacts that result from imprecise instrumentation and sample bleaching.[8,9] Moreover, to adapt a standard wide-field fluorescence microscope for SIM, an additional illumination add-on module is required.

In this letter, we present a generic wide-field optical sectioning scheme, photobleaching imprinting microscopy (PIM). Compared to DM and SIM, wide-field PIM is easy to implement—it does not require knowledge of the system's point-spread-function (PSF) or require an extra illumination module. A depth-resolved image can be simply derived from time-lapse imaging of photobleaching-induced fluorescent decay. The operating principle of wide-field PIM is illustrated in Fig. 1. Upon one-photon excitation, the light intensity measured by a wide-field microscope is the integration of the fluorescence emitted over all depths

$$I(x,y) = C\int \mu_a(x,y,z)F(x,y,z) * PSF_z(x,y)dz, \quad (1)$$

where C is a constant, μ_a is the absorption coefficient of the fluorophore, F is the excitation fluence distribution, PSF_z is the point-spread-function at depth z, and the operator $*$ represents 2D convolution.

In fluorescence microscopy, photobleaching occurs when the excited electrons are trapped in a relatively long-lived triplet state. Compared with a singlet-singlet transition, the forbidden triplet-singlet transition provides a fluorophore with a much longer time to undergo irreversible chemical reactions with the environment.[10] The photobleaching of a fluorophore obeys an exponential temporal decay law

$$\mu_a(t) = \mu_{a0}\exp(-kt), \quad (2)$$

where t is time, μ_{a0} is the initial absorption coefficient of the fluorophore, and k is the photobleaching rate. The photobleaching rate k is a function of excitation fluence F.[11] For one-photon excitation, this relation is described by

$$k = BF. \quad (3)$$

Here B denotes a constant. Since the fluence F is dependent only on z under wide-field excitation, combining Eqs. (1)–(3) gives

$$I(x,y,t) = C\int \mu_{a0}(x,y,z)\exp[-BF(z)t]F(z) * PSF_z(x,y)dz. \quad (4)$$

Equation (4) can be further Taylor expanded as

$$I(x,y,t) = C\sum_{n=0}^{N} t^n \frac{(-B)^n}{n!}\int \mu_{a0}(x,y,z)F^{n+1}(z) * PSF_z(x,y)dz. \quad (5)$$

Polynomial fitting of Eq. (5) gives the coefficient associated with t^n

$$I_n(x,y) = D\int \mu_{a0}(x,y,z)F^{n+1}(z) * PSF_z(x,y)dz, \quad (6)$$

where $D = C(-B)^n/n!$. Since fluence distribution of a high order approaches a delta function $\delta(z - z_0)$, Eq. (6) becomes

[a]C. Li and L. Gao contributed equally to this work.
[b]Author to whom correspondence should be addressed. Electronic mail: lhwang@wustl.edu.

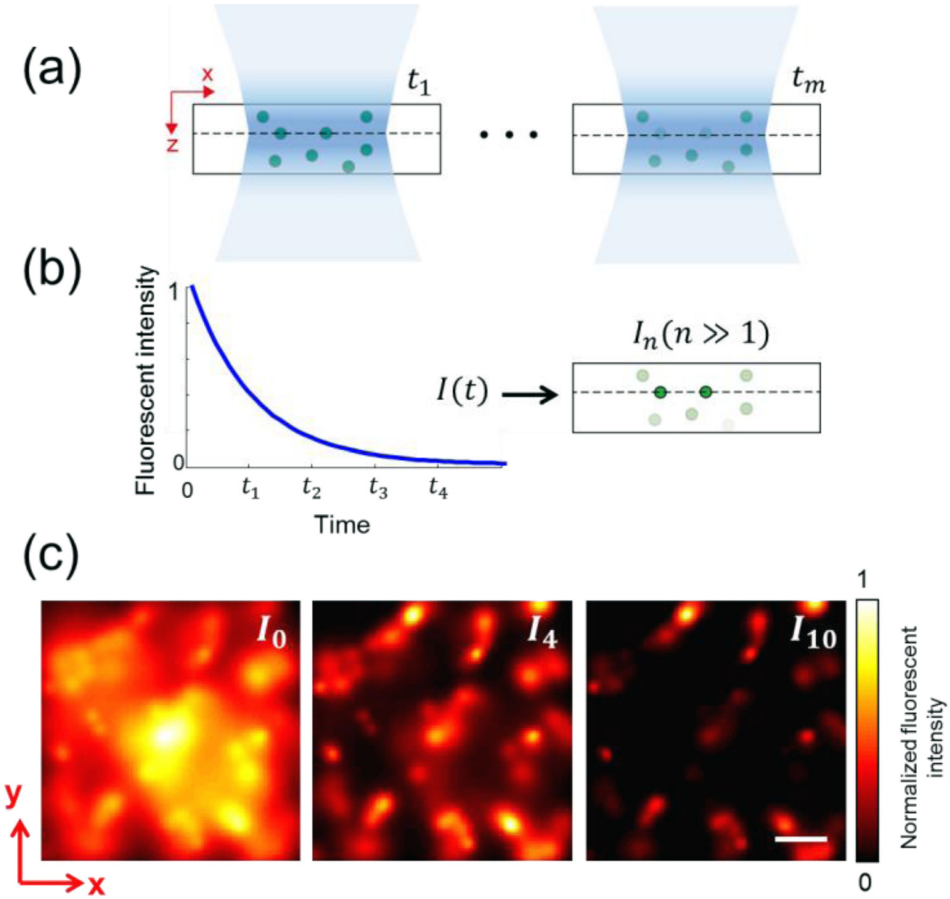

FIG. 1. The operating principle of wide-field PIM. (a) A 3D fluorescent sample is excited by a structured light beam along the depth axis. The fluorophores on the focal plane experience much faster photobleaching than those located out of focus. (b) The polynomial fitting of a fluorescent decay yields the PIM component I_n, which is dependent on the $n+1$ order fluence distribution. (c) Simulated wide-field PIM images (I_0, I_4, and I_{10}) for a 3D sample consisting of randomly distributed fluorescent beads. Here I_0 represents the conventional wide-field fluorescence image, and I_4 and I_{10} represent optically sectioned images. The volume sample has $100 \times 100 \times 100$ (x, y, z) pixels. The lateral and axial optical diffraction limits are 5 pixels and 15 pixels, respectively. The scale bar indicates a 20-pixel length.

$$I_n(x,y,n \gg 1) \approx D\int \mu_{a0}(x,y,z)\delta(z-z_0) * PSF_z(x,y)dz$$
$$= D\mu_{a0}(x,y,z_0) * PSF_{z_0}(x,y), \quad (7)$$

which describes an optically sectioned image at focal plane z_0.

To show optical sectioning in theory, we simulated a case where a volume fluorescent sample was imaged by conventional wide-field fluorescence microscopy and wide-field PIM under one-photon excitation. The numerical simulation was performed with Matlab (R2011a, MathWorks). Randomly distributed point objects were generated inside a 3D cube. The excitation fluence was assumed to be uniform along the lateral axes, and to have a Gaussian profile along the depth axis in the form of

$$F(z) = \exp(-(z-z_0)^2/2\sigma_z^2), \quad (8)$$

where σ_z is correlated to the full width at half maximum (FWHM) of $F(z)$ by FWHM $= 2.35\sigma_z$.

The detection PSF at depth z was considered to have a 2D Gaussian profile

$$PSF_z(x,y) = \exp\left(-\frac{x^2+y^2}{2(2+|z-z_0|)^2}\right). \quad (9)$$

Here the size of the detection PSF reaches a minimum (optical diffraction limit) at the focus $z = z_0$.

Substituting Eqs. (8) and (9) for $F(z)$ and PSF_z into Eq. (4) gives the theoretical photobleaching-induced fluorescent decay $I(t)$ measured by a wide-field detector. The polynomial fitting of $I(t)$ yields the PIM components I_n. As representative images, the wide-field PIM images I_0, I_4, and I_{10} were calculated and are shown in Fig. 1(c). Owing to the nonlinear fluence dependence, the image contrast increases with the order n, implying a gradually decreased section thickness.

Wide-field PIM experiments were carried out on a standard wide-field fluorescence microscope (FV1000, Olympus). The sample was excited by a mercury lamp and imaged by a 100× oil-immersion objective with NA = 1.4 (PlanApo, Olympus). The illumination aperture stop was maximized to assure the NA of the microscope objective was fully utilized for excitation. The excitation light and fluorescence emission were separated by a GFP filter set (excitation, 470–495 nm; emission, 510–550 nm; Olympus). Wide-field fluorescence images were captured by a CCD camera (512×512 pixels, DV412-BV, Andor Technology) which was mounted on the side imaging port of the microscope.

To measure the axial resolution of wide-field PIM, we imaged a single layer of 200 nm diameter fluorescent beads (T14792, Life Technologies). The sample was scanned along the depth axis from the focus to an out-of-focus plane, with a step size of 200 nm. At each depth, a total of 200 time-lapsed frames (0.1 s frame integration time) was acquired. The PIM components I_n associated with different orders of fluence distribution were calculated at a bead's location, and the results are shown in Fig. 2. The FWHM of axial responses $I_0 (\propto F)$, $I_2 (\propto F^3)$, $I_4 (\propto F^5)$, and $I_8 (\propto F^9)$ are 1.25 μm, 0.43 μm, 0.30 μm, and 0.23 μm, respectively. By taking the

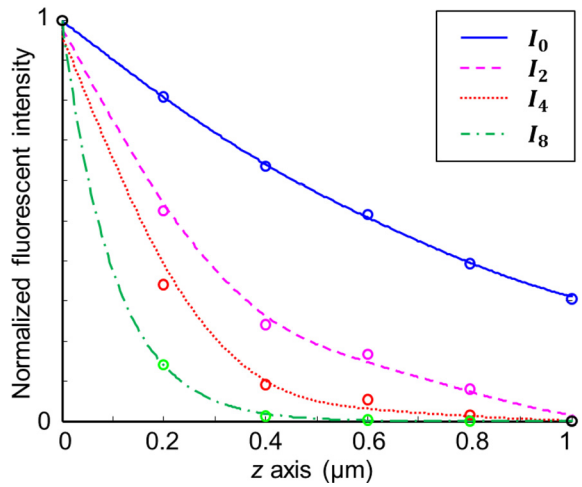

FIG. 2. Measurement of axial responses associated with PIM components $I_0(\propto F)$, $I_2(\propto F^3)$, $I_4(\propto F^5)$, and $I_8(\propto F^9)$. Here F denotes the excitation fluence.

geometrical size of a fluorescent bead into consideration, the axial resolutions associated withI_0, I_2, I_4, and I_8 approximate 1.15 μm, 0.33 μm, 0.20 μm, and 0.13 μm, respectively. As expected, a higher order dependence on the excitation fluence led to a higher axial resolution.

To demonstrate the optical sectioning capability of wide-field PIM in biological tissue, we imaged a mouse kidney section ~16 μm thick. The glomeruli and convoluted tubules were labeled with Alexa Fluor 488 (495 nm excitation peak, 519 nm emission peak). First, a conventional wide-field fluorescence image was captured. As shown in Fig. 3(a), the fluorescent basal cell infoldings of the kidney tubules were blurred in the image due to the out-of-focus light. Then, after acquiring 80 time-lapse fluorescence images (0.1 s frame integration time), the PIM image associated with I_4, which is proportional to the fifth order of fluence distribution, was derived and is shown in Fig. 3(b) The background fluorescence has been substantially reduced due to nonlinear fluence dependence, thereby resulting in a clear in-focus image of the striation structure. It is worth noting that here we used the PIM component I_4 instead of a higher order. A higher order PIM image can be extracted normally at the expense of increasing the number of temporal samplings and the extent of photobleaching. As indicated by Fig. 2, the gain in the axial resolution by using I_8 (0.13 μm) compared to using I_4 (0.2 μm) is moderate. However, to extract these coefficients from a time-lapse fluorescent decay, a total of only 80 images were captured for deriving I_4, compared to 200 images required for deriving I_8.

Since a competing technique, deconvolution microscopy, has also been used in background reduction in wide-field fluorescence microscopy,[2] here we compare it with wide-field PIM in the context of image contrast. The wide-field fluorescence image (Fig. 3(a)) was deconvolved with the theoretically calculated PSF. The deconvolution was performed along the depth axis, and the resulting images were processed by the "no neighbors" method.[12] The deconvolved in-focus image is shown in Fig. 3(c). The intensity profiles across the dashed line in Figs. 3(a)–3(c) are shown in Fig. 3(d), indicating an approximately six-fold improvement in image contrast achieved by wide-field PIM over deconvolution image processing.

Furthermore, to acquire a 3D volume image, we scanned the tissue sample along the depth axis with a step size of 2 μm. At each depth, a total of 80 time-lapse fluorescence images (0.1 s frame acquisition time) was captured for PIM calculation. The 3D images acquired by conventional wide-field fluorescence microscopy and wide-field PIM are shown in Figs. 4(a) and 4(b), respectively. Representative images acquired at depths $z = 0$, 4 μm, 8 μm, and 12 μm are shown in Fig. 4(c). Due to crosstalk from adjacent depth layers, the contrast in the 3D wide-field fluorescence image was low. While in the 3D wide-field PIM image, owing to optical sectioning along the depth axis, the striation structure became

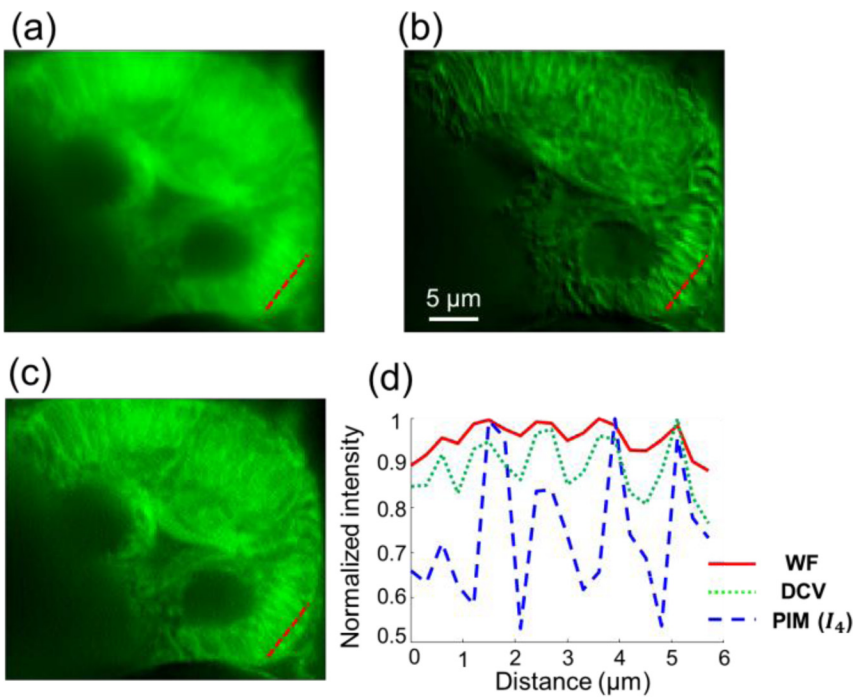

FIG. 3. A comparison of (a) a conventional wide-field image, (b) a wide-field PIM image ($I_4 \propto F^5$), and (c) a deconvoluted wide-field image of a mouse kidney tissue section. In the sample, the glomeruli and convoluted tubules were labeled with Alexa Fluor 488. (d) Intensity profiles across the dashed line in a–c. WF, wide-field fluorescence; DCV, deconvolution.

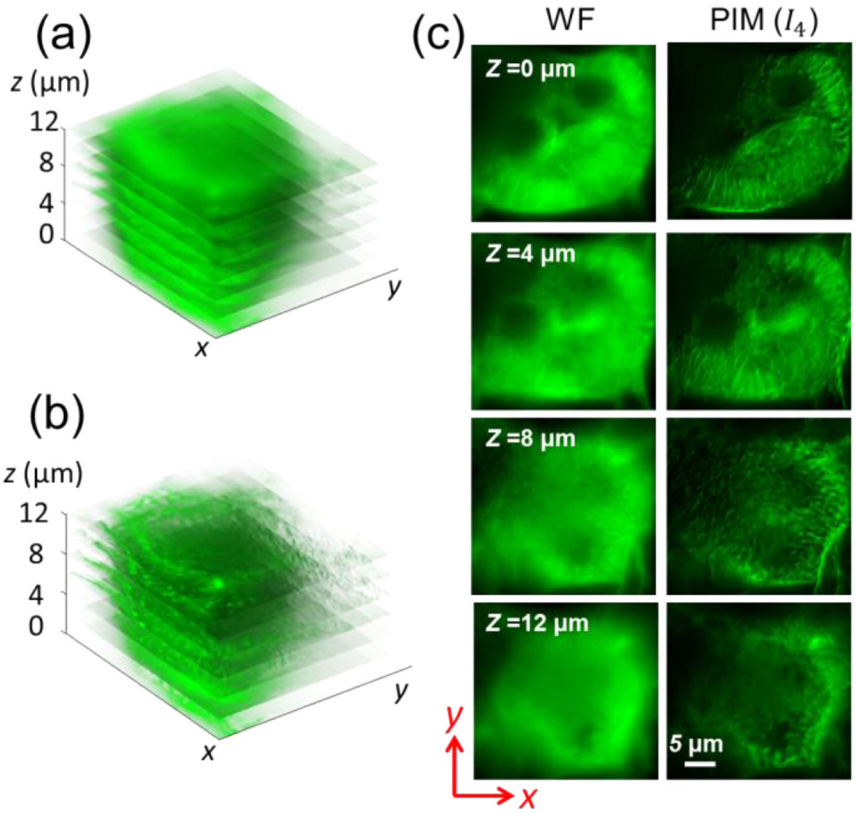

FIG. 4. Three-dimensional volume imaging of a mouse kidney tissue section by (a) conventional wide-field fluorescence microscopy and (b) wide-field PIM (I_4). In the sample, the glomeruli and convoluted tubules were labeled with Alexa Fluor 488. The sample was scanned along the depth axis with a step size of 2 μm. (c) Representative images acquired at depth layers $z = 0$, 4 μm, 8 μm, and 12 μm.

more distinguishable. In addition, since wide-field PIM relies on fluorescence decay to extract the nonlinear components, we evaluated the gain in optical sectioning against the loss of fluorescence intensity level after the PIM procedure. A measurement showed that the tissue's fluorescent intensity was decreased by ~15% due to photobleaching after acquiring a depth layer.

In summary, we presented a generic wide-field optical sectioning scheme, wide-field PIM, with a submicron axial resolution. Compared to other depth-resolved wide-field imaging techniques, wide-field PIM is easier to implement on a standard fluorescence microscope and does not depend on specific illumination modules. We showed that wide-field PIM can significantly reduce the out-of-focus light in tissue fluorescence imaging, thereby considerably improving the image contrast. Furthermore, the volume imaging capability of wide-field PIM was also demonstrated, revealing 3D structures that were obscured by the background fluorescence under a wide-field acquisition.

This work was sponsored in part by National Institutes of Health (NIH) grants DP1 EB016986 (NIH Director's Pioneer Award), R01 EB008085, R01 CA134539, U54 CA136398, R01 CA157277, and R01 CA159959. L.W. has a financial interest in Microphotoacoustics, Inc. and Endra, Inc., which, however, did not support this work.

[1]J. W. Lichtman and J. A. Conchello, Nat. Methods **2**(12), 910–919 (2005).
[2]J. G. McNally, T. Karpova, J. Cooper, and J. A. Conchello, Methods **19**(3), 373–385 (1999).
[3]J. M. Murray, Cold Spring Harb Protoc 2011 **12**, 1399–1437 (2011).
[4]W. Wallace, L. H. Schaefer, and J. R. Swedlow, BioTechniques **31**(5), 1076 (2001).
[5]L. Gao, N. Bedard, N. Hagen, R. T. Kester, and T. S. Tkaczyk, Opt. Express **19**(18), 17439–17452 (2011).
[6]M. A. A. Neil, R. Juskaitis, and T. Wilson, Opt. Lett. **22**, 1905 (1997).
[7]N. Hagen, L. Gao, and T. S. Tkaczyk, Opt. Express **20**(1), 403–413 (2012).
[8]L. H. Schaefer, D. Schuster, and J. Schaffer, J. Microsc. **216**(2), 165–174 (2004).
[9]D. Karadaglic and T. Wilson, Micron **39**(7), 808–818 (2008).
[10]R. Y. Tsien, L. Ernst, and A. Waggoner, *Handbook of Biological Confocal Microscopy*, edited by J. B. Pawley (Springer, 2006).
[11]G. H. Patterson and D. W. Piston, Biophys. J. **78**(4), 2159–2162 (2000).
[12]J. R. Monck, A. F. Oberhauser, T. J. Keating, and J. M. Fernandez, J. Cell Biol. **116**(3), 745–759 (1992).